High−Resolution Crystal Structure of Manganese Peroxidase: Substrate and Inhibitor Complexes † , ‡

4 AUTHORS, INCLUDING:

Heather Youngs
University of California, Berkeley
29 PUBLICATIONS **1,763** CITATIONS

SEE PROFILE

Michael H Gold
Tennessee Clinical Research Center
269 PUBLICATIONS **12,051** CITATIONS

SEE PROFILE

Thomas L Poulos
University of California, Irvine
164 PUBLICATIONS **4,548** CITATIONS

SEE PROFILE

High-Resolution Crystal Structure of Manganese Peroxidase: Substrate and Inhibitor Complexes[†,‡]

Munirathinam Sundaramoorthy,*,[§] Heather L. Youngs,[‖,⊥] Michael H. Gold,[‖] and Thomas L. Poulos[@]

Division of Nephrology, Department of Medicine, Center for Matrix Biology, and Department of Biochemistry, Vanderbilt University Medical Center, Nashville, Tennessee 37232-2372, Department of Biochemistry and Molecular Biology, OGI School of Science and Engineering, Oregon Health and Sciences University, Portland, Oregon 97291-1000, and Departments of Molecular Biology and Biochemistry, Physiology and Biophysics, and Chemistry and Center in Chemical and Structural Biology, University of California, Irvine, California 92697-3900
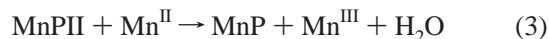
Received December 21, 2004; Revised Manuscript Received March 1, 2005

ABSTRACT: Manganese peroxidase (MnP) is an extracellular heme enzyme that catalyzes the peroxide-dependent oxidation of Mn^{II} to Mn^{III}. The Mn^{III} is released from the enzyme in complex with oxalate. One heme propionate and the side chains of Glu35, Glu39, and Asp179 were identified as Mn^{II} ligands in the 2.0 Å resolution crystal structure. The new 1.45 Å crystal structure of MnP complexed with Mn^{II} provides a more accurate view of the Mn-binding site. New features include possible partial protonation of Glu39 in the Mn-binding site and glycosylation at Ser336. This is also the first report of MnP−inhibitor complex structures. At the Mn-binding site, divalent Cd^{II} exhibits octahedral, hexacoordinate ligation geometry similar to that of Mn^{II}. Cd^{II} also binds to a putative second weak metal-binding site with tetrahedral geometry at the C-terminus of the protein. Unlike that for Mn^{II} and Cd^{II}, coordination of trivalent Sm^{III} at the Mn-binding site is octacoordinate. Sm^{III} was removed from a MnP−Sm^{III} crystal by soaking the crystal in oxalate and then reintroduced into the binding site. Thus, direct comparisons of Sm^{III}-bound and metal-free structures were made using the same crystal. No ternary complex was observed upon incubation with oxalate. The reversible binding of Sm^{III} may be a useful model for the reversible binding of Mn^{III} to the enzyme, which is too unstable to allow similar examination.

White-rot basidiomycetous fungi are the only organisms capable of degrading the phenylpropanoid, plant cell wall polymer, lignin (*1−4*). The lignin-degrading system of these fungi also can oxidize a variety of economically and environmentally important aromatic pollutants (*5−9*). Under ligninolytic conditions, the best-studied lignin-degrading fungus, *Phanerochaete chrysosporium*, secretes two families of extracellular heme peroxidases, lignin peroxidase (LiP) and manganese peroxidase (MnP)[1] (*2−4, 10*), and a hydrogen peroxide-generating system (*2, 4, 6*).

MnP from *P. chrysosporium* has been studied extensively by a variety of biochemical and biophysical methods (*11−15*). The crystal structure illustrates that the heme environ-

ment of MnP is similar to that of other plant and fungal peroxidases (*16*). However, MnP is the only heme peroxidase capable of the one-electron oxidation of Mn^{II} in a typical peroxidase reaction cycle:

$$MnP + H_2O_2 \rightarrow MnPI + H_2O \tag{1}$$

$$MnPI + Mn^{II} \rightarrow MnPII + Mn^{III} \tag{2}$$

$$MnPII + Mn^{II} \rightarrow MnP + Mn^{III} + H_2O \tag{3}$$

where MnPI and MnPII are the oxidized intermediates MnP compounds I and II, respectively.

The 2.0 Å resolution crystal structure of MnP, determined at room temperature, shows that the substrate, Mn^{II}, binds to one heme propionate and the side chains of three amino acids, Glu35, Glu39, and Asp179, as well as two solvent ligands (*16*) (Figure 1). This site was confirmed by kinetic and biophysical studies of wild-type MnP and of proteins containing point mutations in the putative binding site.

[1] Abbreviations: MnP, manganese peroxidase; MnP−Mn^{II}, manganese−enzyme complex; MnP−Cd^{II}, cadmium−enzyme complex; MnP−Sm^{III}, samarium−enzyme complex; 1MNP, 2.0 Å room-temperature MnP−Mn^{II} crystal structure; MNPMN, 1.45 Å cryo-treated MnP−Mn^{II} crystal structure; MNPSM, MnP−Sm^{III} crystal structure; MNPSMOX, MnP−Sm^{III} crystal soaked in oxalate; MNPOXSM, structure of MnP−Sm^{III} crystal soaked in oxalate and then incubated with $SmCl_3$; CGLS, conjugate gradient least squares.
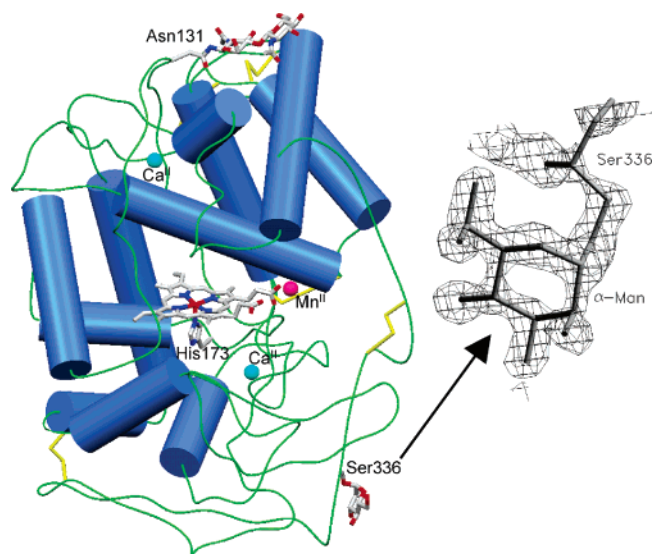
FIGURE 1: Overall structure of MnP−Mn^{II} refined at 1.45 Å resolution. A second glycosylation site at Ser336 with O-linked α-mannose is shown. The $F_o - F_c$ omit map around Ser336 is contoured at 3.0σ showing density for α-mannose. This is a new feature in the 1.45 Å cryo map that was not present in the 2.0 Å room-temperature structure.

Alteration of the proposed ligands in the Mn-binding site significantly affects Mn binding and oxidation (*17−22*), and crystals of both the single variant, D179N, and the double variant, E35Q/D179N, lack electron density at the proposed Mn-binding site (*23*), suggesting that Mn^{II} is not bound.

MnP is unique among enzymes using manganese as a redox cofactor. Rather than permanently sequestering Mn^{II} in an interior binding site, MnP selectively binds Mn^{II} on the surface of the protein, oxidizes it, and then releases the Mn^{III} product in complex with organic acids such as oxalate and malonate. The relatively stable Mn^{III}−organic acid complex acts as a diffusible mediator to oxidize the terminal phenolic substrate lignin (*24−26*). In the absence of Mn^{II}, MnP intermediates can directly oxidize small phenolic substrates, such as guaiacol and dimethoxyphenol, but only at very slow rates, insufficient for enzyme turnover (*13, 27−29*). Whether a Mn^{II}−chelator complex binds to the enzyme to form a ternary complex or the chelator simply facilitates release of Mn^{III} via ligand displacement has not been completely resolved. However, the crystal structure of MnP−Mn^{II} in the absence of chelators suggests that the later alternative is more likely (*14, 16, 27, 30, 31*).

The Mn-binding site of MnP has been extensively studied by site-directed mutagenesis. Flexibility of the Mn-binding site is suggested by the multiple conformations of the ligands, Glu35 and Glu39 in both the D179N single variant and E35Q/D179N double variant crystal structures (*23*). However, molecular modeling and kinetic studies indicate that Mn^{II} binding and oxidation are sensitive to subtle changes in ligand geometry (*17−21*). These effects were studied by altering the amino acids in the active site. Competition for ligands using other metal ions is an alternative method for studying the intact binding site. Indeed, the flexibility of the Mn-binding site in MnP allows a wide variety of metal ions to bind. However, it appears that only Cd^{II} exhibits a dissociation constant similar to that of Mn^{II} (*19*), and other divalent cations, such as Co^{II} (*32*), Fe^{II}, and Zn^{II}, exhibit poor

binding (H. L. Youngs and M. H. Gold, unpublished results). Trivalent cations such as the lanthanides Sm^{III} and Eu^{III} also competively inhibit Mn^{II} oxidation (H. L. Youngs and M. H. Gold, unpublished results), and ^{1}H NMR studies showed binding of Ce^{III} and Gd^{III} to the MnP active site (*30*). The stable lanthanides, therefore, have been proposed to mimic the binding of Mn^{III} (*30*). While it is attractive to use these metals in functional studies of MnP, the lanthanides have a much larger mass-to-charge ratio and larger ionic radii, tend to accept more ligands, and adopt a much wider variety of ligation geometries than Mn^{III} (*33*). Thus, a detailed crystallographic examination of the Mn-binding site and interaction with other metals should provide information that is useful for kinetic and biophysical studies.

In this work, we present a refined wild-type MnP−substrate model (1.45 Å cryo data set), as well structures of complexes with inhibitors Cd^{II} and Sm^{III} (1.6 Å), and of a metal-free MnP obtained by oxalate chelation of Sm^{III} from the Sm^{III}−MnP complex (1.6 Å). The results presented here provide a more accurate model of native MnP at very high resolution, a structural basis for MnP inhibition with non-oxidizable metal ions, and direct structural evidence for the removal of a higher-oxidation-state metal ion from the enzyme by organic acid chelators.

MATERIALS AND METHODS

Protein Purification and Crystallization. Wild-type MnP was purified from shaking cultures of *P. chrysosporium* grown on high-carbon, low-nitrogen medium as previously described (*12, 13, 19*). Crystals of MnP−Mn^{II}, MnP−Cd^{II}, and MnP−Sm^{III} were grown using the hanging drop vapor diffusion method as described previously (*34*). The reservoir contained 30% (w/v) polyethylene glycol 8000, 0.2 M ammonium sulfate, and 0.1 M sodium cacodylate buffer (pH 6.5). The crystallization drops were composed of 5 μL of the protein solution (10−15 mg/mL) mixed with an equal volume of the reservoir solution. The crystallization was initiated by a seeding procedure, using serially diluted seed stocks prepared from the old native MnP crystals. High-dilution seed stocks resulted in fewer big crystals in the protein drops, circumventing the need for macroseeding, used in our previous studies (*16, 23*). MnP−Mn^{II} crystals were grown with an excess of MnCl$_2$ (4 mM) at room temperature. MnP−Cd^{II} and MnP−Sm^{III} crystals were grown at 4 °C with an excess (4−5 mM) of CdCl$_2$ and SmCl$_3$, respectively, over a period of 4−8 weeks.

Data Collection and Processing. Crystals were harvested in a synthetic mother liquor identical to the reservoir solution and transferred to the cryo solution containing 10% (v/v) glycerol in the mother liquor. The cryo-soaked crystals were flash-frozen in a liquid N$_2$ stream, and all data sets were collected at −160 °C. The wild-type data set was collected using a Siemens area detector system using a rotating Siemens anode X-ray source and short Supper mirrors. The frames were integrated and merged using XENGEN (*35*) to obtain the 1.45 Å MNPMN data set (Table 1).

The MnP−Cd^{II} and MnP−Sm^{III} data sets were collected using an R-Axis IV imaging plate system and a Rigaku rotating anode X-ray source equipped with Yale mirrors. The data sets were integrated and scaled using DENZO and SCALEPACK from the HKL suite (*36*). A single MnP−

Table 1: Summary of Crystallographic Data Collection and Refinement

	MNPMN	MNPCD	MNPSM	MNPSMOX	MNPOXSM
no. of data observed	224749	173448	178491	157537	127445
no. of unique reflections	65426	47574	48896	44812	37351
R_{sym} (%)	7.18	6.1	5.8	4.3	6.9
highest resolution (Å)	1.45	1.6	1.6	1.6	1.7
$I/\sigma(I)$ at the highest resolution	1.1	2.6	3.0	2.2	1.3
completeness (%)					
overall	97	96	98	89	89
highest-resolution shell	82	64	80	55	63
resolution range (Å)	8.0–1.45	8.0–1.6	8.0–1.6	8.0–1.6	8.0–1.7
no. of reflections [$F_o > 4\sigma(F)$]	61836 (46646)	42371 (35252)	43561 (37026)	39872 (33286)	33184 (25520)
R_{cryst} ($F_o > 4\sigma$)	0.18 (0.141)	0.166 (0.146)	0.164 (0.149)	0.166 (0.148)	0.167 (0.14)
R_{free} ($F_o > 4\sigma$)	0.226 (0.186)	0.225 (0.204)	0.22 (0.20)	0.228 (0.203)	0.243 (0.210)
rms deviation					
1–2 distance (Å)	0.012	0.009	0.009	0.008	0.007
1–3 distance (Å)	0.027	0.023	0.023	0.023	0.022

Cd^{II} crystal was used to collect the MNPCD data set. Three data sets were collected with a single $MnP–Sm^{III}$ crystal. A long crystal was carefully cut into two pieces, and the first piece was used to collect the complete data set (MNPSM). The second piece of the same crystal was soaked in 10 mM sodium oxalate for ~1 h by stepwise addition to the cryo solution. This crystal was used to collect a complete data set (MNPSMOX). The crystal was retrieved after data collection and thawed in the oxalate-free cryo solution at room temperature. Aliquots of a $SmCl_3$ solution were subsequently added to a final concentration of 4 mM. The crystal, resoaked in Sm^{III}, was refrozen, and a complete data set (MNPOXSM) was collected. The data collection statistics for all the data sets are given in Table 1.

Refinement. Initial stages of refinement of the $MnP–Mn^{II}$ structure were performed using XPLOR (*37*). The 2.0 Å room-temperature structure (PDB entry 1MNP) was used as the starting model in the refinement. Since the frozen crystal is nonisomorphous with the room-temperature crystal, rigid body refinement was carried out using 30.0–3.0 Å data, which resulted in an R_{cryst} of 30%. This was followed by a three-step refinement using simulated annealing at 3000 K, 120 cycles of conjugate gradient least squares (CGLS), and 20 cycles of individual B-factor refinement protocols (8.0–2.5 Å reflections; R_{cryst} = 19%, and R_{free} = 23%). No manual model adjustment was made until this stage. As the resolution was increased beyond 2.0 Å, manual adjustments of models were made when necessary. Many branched amino acid side chains were changed to correct rotamer conformation, and multiple conformers were modeled, guided by the $F_o − F_c$ and $2F_o − F_c$ maps. A new glycosylation site at Ser336 was identified, and a mannose was modeled at this site. As the resolution approached 1.45 Å, additional solvent sites and three glycerol molecules were modeled. Strong electron density persisted at two sites in the solvent region with no potential interactions with protein atoms. These sites could not be modeled with glycerol, sulfate, or cacodylate molecules present in the crystallization and cryo solutions, and were modeled as water molecules. At this stage, R_{cryst} and R_{free} equaled 18.4 and 20.4%, respectively.

When the X-PLOR refinement converged, further refinement was continued using SHELXL (*38*) with the intensity data, including negative intensity values. The same working and test sets of reflections used in X-PLOR were maintained in the SHELXL refinement. The SHELXL restraints for hetero groups were derived from X-PLOR restraints. The

metal–ligand distances for Fe^{III}, Ca^{II}, and Mn^{II}, however, were not restrained. After extensive refinement using the CGLS protocol, some manual adjustment, and a more complete solvent model, R_{cryst} and R_{free} converged to 14 and 18.6%, respectively (for $F_o > 4\sigma$), for isotropic B-factor refinement. Attempts to refine anisotropic B-factors were not successful. Even though the data-to-parameter ratio was slightly greater than 2, a 3% drop in R_{cryst} was not supported by a similar drop in R_{free}, which remained virtually at the same level as in the isotropic B-factor refinement of the previous cycle.

The $MnP–Cd^{II}$ and $MnP–Sm^{III}$ structures were refined entirely using SHELXL. The refined wild-type MnP structure, excluding the Mn^{II} ion, was used as the starting model in all the difference Fourier calculations. The refinements were cross-validated following R_{free}, using the same subset of reflections, as in the case of $MnP–Mn^{II}$. The appropriate metal ions, ligands, and solvent structures were remodeled using $2F_o − F_c$ and $F_o − F_c$ maps calculated using respective data sets. The metal–ligand distances were not restrained during the refinement. All the model building was carried out using the TOM-FRODO map fitting graphics software (*39*), and figures were prepared using SETOR (*40*).

RESULTS AND DISCUSSION

MnP–Mn^{II} Structure at 1.45 Å Resolution. The MnP–Mn^{II} crystals, when frozen in a liquid N_2 stream, diffract to significantly higher resolution than room-temperature crystals. The unit cell volume is reduced by ~4% under cryo conditions, and the new unit cell dimensions are as follows: $a = 160.97$ Å, $b = 45.42$ Å, $c = 52.93$ Å, and $\beta = 96.9°$ (space group $C2$). A complete data set was acquired at 1.45 Å resolution using an in-house X-ray source. The 2.0 Å room-temperature model was used as the starting model for refinement against the new data. The high-resolution map (MNPMN) reveals several important structural features. When the resolution is increased beyond 1.8 Å, the electron density map reveals correct rotamer conformations for many branched amino acid side chains. Several side chains exhibit multiple conformations. The higher-resolution map also reveals ordered density for a second glycosylation site at Ser336, which was modeled as α-mannose (Figure 1). The previously identified N-glycosylation site at Asn131 shows additional electron density, which may be due to the presence of a third sugar residue. When this density is modeled as
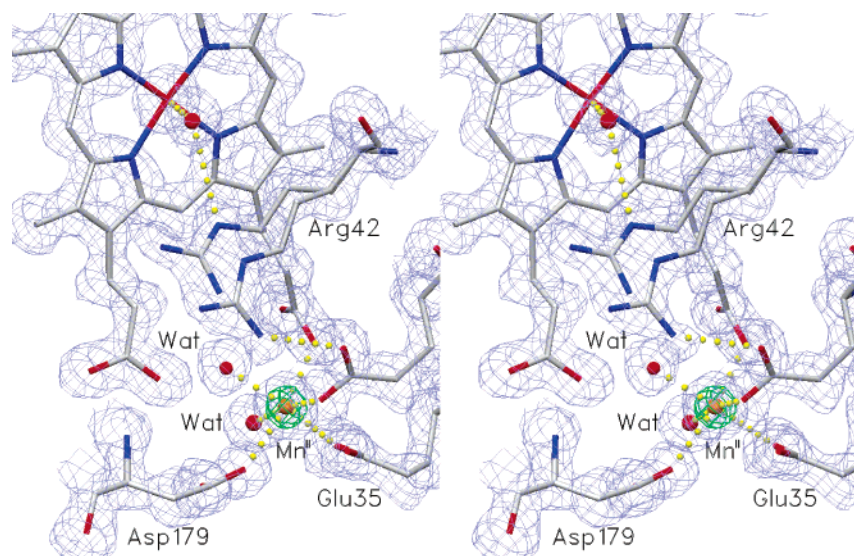
FIGURE 2: Stereo representation of the MnP−Mn^{II} active site. The $2F_o - F_c$ omit map calculated at 1.45 Å and contoured at 1σ shows well-defined density for the heme, Mn^{II}, and its ligands, including two solvent molecules, and the $F_o - F_c$ omit map contoured at 25σ (green) shows a strong peak at the Mn-binding site. Active site residue Arg42 is shown in two conformations, native and compound I (see the text for the definition of these terms).

Table 2: Metal−Ligand Distances (Å)

	Mn^{II} (wild-type MNP)	Cd^{II} (MNPCD)	Sm^{III} (MNPSM)	H$_2$O (MNPSMOX)	Sm^{III} (MNPOXSM)
Mn-binding site					
heme O1D	2.15	2.22	2.30		2.30
Glu35 OE1	2.41	2.31	2.48	3.07	2.56
Glu39 OE1	2.07	2.31, 2.39	2.36		2.54
Asp179 OD1	2.40	2.34	2.44	2.45	2.47
Wat1	2.23	2.41	2.45	2.84	2.54
Wat2	2.29	2.33	2.51	3.23	2.60
Wat3			2.49		2.82
Wat4			2.93		3.18
Fe−ligand distances					
Fe−His173 NE2	2.17	2.14	2.13	2.13	2.25
Fe−distal water	2.28	2.03	2.10	1.8	2.11

α-mannose, it refines with high *B*-factors and, hence, was excluded from further refinement. At least three ordered glycerol sites were identified in the difference Fourier maps, which were occupied by water molecules in the original room-temperature structure. Despite a significant increase in resolution, small portions of the main chain and a few surface side chains are still disordered with poorly defined density. Most notably, the disordered C-terminal loop near the Mn-binding site does not show any improvement. The dynamic disorder of this loop close to the heme propionates may be associated with the accessibility of the substrate-binding site.

The active site is well-defined in the high-resolution maps, including a $>25\sigma$ density in the $F_o - F_c$ omit map (Figure 2). All six Mn^{II} ligands are well-defined, and the metal−ligand distances are shorter compared to those in the 2.0 Å structure (Table 2). A new significant feature of the ligands is a peak 1.4 Å from the unliganded carboxyl oxygen of Glu39, a feature not found for the other Mn^{II} ligands. Distal residue Arg42 exhibits multiple conformations, a major one close to Glu39 and a minor one close to the distal side coordination position. The distance between OE2 of Glu39 and NH1 of Arg42 in the major conformation is 2.4 Å, and the new peak between the two atoms makes an angle of 110°, indicative of protonation of Glu39. This may be partly responsible for the reduction of net negative charge in the

Mn-binding site in the native state, and this conformation of Arg42 is termed "native". The distal arginine has been shown to move closer to the oxyferryl center to stabilize the enzyme intermediate in the crystal structure of cytochrome *c* peroxidase compound I (*41*). Hence, the minor conformation of Arg42 close to the distal side coordination position is designated as the "compound I" state. Thus, Arg42 might play two roles in MnP, stabilizing Mn^{II} binding in the native state and stabilizing the oxyferryl species in compound I, while reducing the stability of Mn$^{II/III}$ binding for its release upon oxidation.

MnP−Cd^{II} Structure. Previously, we reported the crystal structures of a D179N single mutant and an E35Q/D179N double mutant of MnP, which are deficient in Mn^{II} binding (*17, 18, 23*), and modeling and kinetic studies of an E39D mutant (*21*). These studies indicated flexibility of the Mn-binding site, as evidenced by the multiple conformations of Glu35 and Glu39. Hence, the Mn-binding site may accommodate metals with different ionic radii, provided the metals accept carboxylate ligands. The ionic radius of Mn^{II} is 0.83 Å, and that of Cd^{II} is 0.95 Å when hexacoordinated (*42*). There is evidence that Cd^{II} can substitute for Mn^{II} in other enzymes, such as photosystem II (*43*) and a Mn^{II}-dependent protein serine phosphatase (*44*). Similarly, Cd^{II} effectively competes with Mn^{II} in Mn^{II}-specific transport systems (*45−47*).
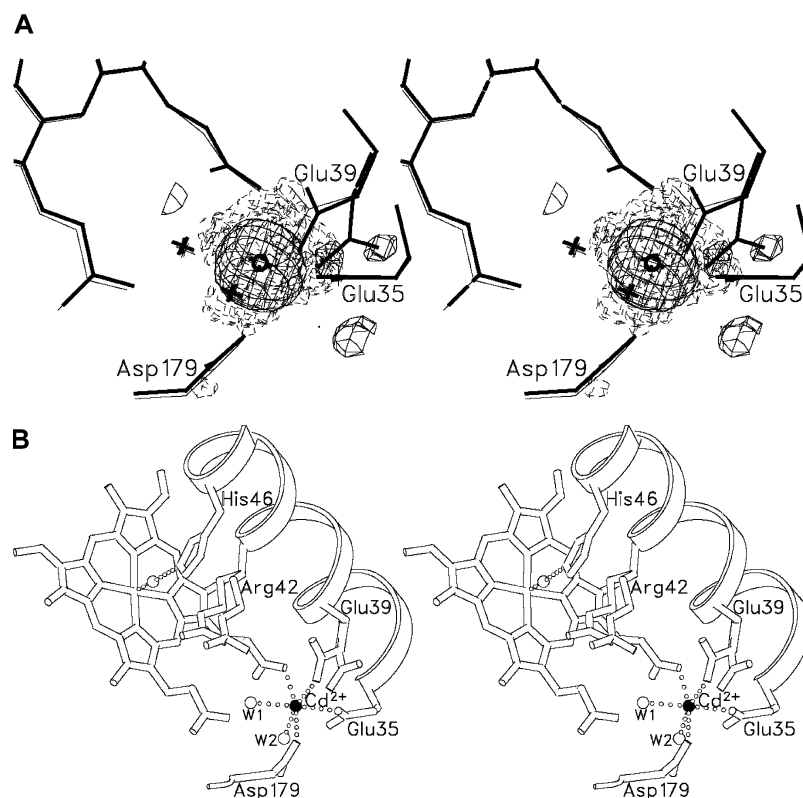
FIGURE 3: (A) Stereoview of the $F_o - F_c$ map at the Mn-binding site. The map was calculated using the MNPCD data set and the MnP−Mn[II] model without Mn[II]. The models of both MnP−Mn[II] (thin lines) and refined MnP−Cd[II] (thick lines) are superimposed. The map is contoured at $\pm 3\sigma$, and the positive peak is stronger than 40σ. (B) Stereoview of the Cd[II]-bound structure near the Mn-binding site. The metal is still hexacoordinated, but the ligands have moved compared to those in the Mn[II]-bound structure, notably, the two conformations of Glu39.

Previously, we reported extensive characterization of the effects of Cd[II] on manganese peroxidase as a reversible, competitive inhibitor (19). Steady-state kinetic analysis showed that Cd[II] is uncompetitive for H_2O_2 and MnP−Cd[II] forms compound I under transient-state conditions. Cadmium cannot be oxidized by MnP intermediates and acts as a reversible, competitive inhibitor for Mn[II] oxidation with a K_i of 10 μM. Similar changes in the MnP heme spectrum upon binding of Cd[II] and Mn[II] and very close apparent dissociation constants ($K_d \approx 8$ μM for Cd[II] and 10 μM for Mn[II]) indicate that these metals bind at the same site. Finally, Cd[II] inhibits the reduction of compounds I and II by Mn[II], but not by organic substrates which bind to alternate sites, suggesting specific binding of Cd[II] at the Mn-binding site.

Growth of MnP crystals in the absence of Mn[II] is severely affected, resulting in bleaching due to possible loss of heme at room temperature as observed for Mn[II]-free wild-type and mutant proteins (23). MnP−Cd[II] exhibits behavior similar to that of Mn[II]-free MnP when crystallized at low temperatures, and when grown at 4 °C, the crystals remain dark brown even though they grow slowly. The fully grown MnP−Cd[II] crystals diffract to better than 1.6 Å resolution under cryogenic conditions. The $F_o - F_c$ map calculated using the 1.45 Å MnP−Mn[II] structure, excluding Mn[II] and its ligands, revealed >40σ density at the Mn-binding site (Figure 3). This site is modeled as Cd[II], hexacoordinated to Glu35, Glu39, Asp179, a heme propionate, and two water molecules in a manner similar to that of Mn[II] in the MnP−Mn[II] structure (Figure 2). The ligand geometry is the same as for Mn[II], although the ligand distances differ slightly for

the two metals (Table 2). Another conserved feature is the hydrogen bond between Arg177 and Glu35 (20). However, Glu39 exhibits two conformations in this structure, and Cd[II] is coordinated in both conformations. In contrast, Glu39 does not interact with Arg42 in either of the conformations. The lack of a Glu39−Arg42 interaction in the MnP−Cd[II] structure increases the net negative charge, which might be responsible for tighter binding of Cd[II] than of Mn[II]. Other subtle differences in the solvent structure of MnP−Cd[II] compared to MnP−Mn[II] were observed.

The MnP−Cd[II] structure also exhibits a possible additional metal-binding site near the C-terminus (Figure 4). The carboxy-terminal oxygen, the side chain of Asp84, and two solvent molecules provide ligands to a second cadmium ion, displaying tetrahedral geometry. Ligands in the two metal sites, Glu39 and Asp84, are linked through hydrogen bonds mediated by Asp85 and water. This network of hydrogen bonds is possible only with the open conformation of Glu39. Although Mn[II] is not observed to bind at this site in the crystal structures, a second, lower-affinity Mn-binding site has been postulated on the basis of pH binding analysis of the protein in solution (48). It is possible that Mn[II] does bind to this site under physiological conditions, but not under the conditions for crystal formation (pH 6.5 in cacodylate buffer). The site is exposed to the solvent and could accommodate a Mn[II] ion with a bound chelator such as oxalate or malonate. Alternatively, Cd[II] may exhibit a higher affinity for this site than Mn[II] because of its larger mass-to-charge ratio and its ability to adopt a wider range of ligation geometries (33). Atomic absorption analysis indicated only 1 equiv of Cd[II]
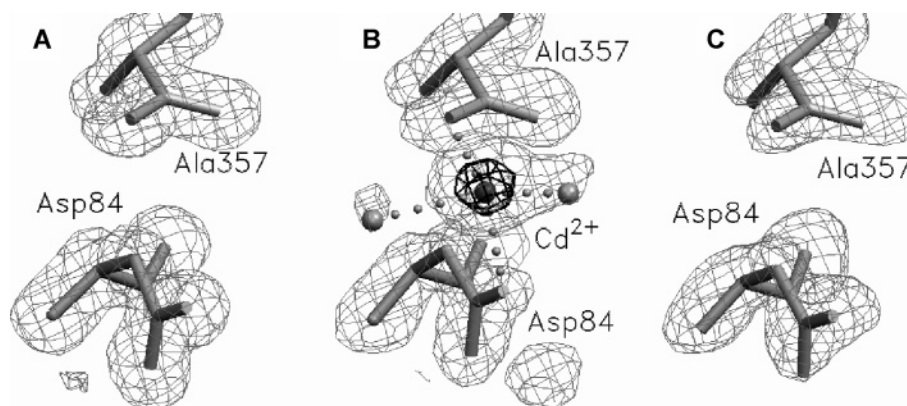
FIGURE 4: Comparison of the C-termini of MnP−Mn[II], MnP−Cd[II], and MnP−Sm[III] structures. The $F_o − F_c$ omit maps were calculated omitting all atoms near the C-terminus within a sphere with a radius of 5 Å, including Ala357 and Asp84. The density is contoured at 3σ for MnP−Mn[II] (A) and MnP−Sm[III] (C) and 3σ and 20σ for MnP−Cd[II] (B). The large peak in the MnP−Cd[II] map is modeled as Cd[II], and its four potential ligands include the terminal carboxylate of the polypeptide, Ala357, and the side chain carboxylate of Asp84.

binding per mole of protein in solution, possibly due to partial occupation of both sites by this metal at pH 4.5 (*19*).

MnP−Sm[III] and Metal-Free MnP Structures. Like MnP−Cd[II] crystals, MnP−Sm[III] crystals were grown at 4 °C and diffract to 1.6 Å under cryo conditions. Three data sets were collected using a single crystal (Table 1). The first data set (MNPSM) collected with the first half of the crystal exhibited >35 σ density at the Mn-binding site in the $F_o − F_c$ map calculated using the MnP−Mn[II] coordinates, excluding Mn[II] and its ligands (Figure 5A). The site was modeled with a Sm[III] ion, and the structure was refined (Table 1). Unlike the MnP−Mn[II] and MnP−Cd[II] structures, the metal site in MnP−Sm[III] is coordinated with eight ligands (Table 2 and Figure 5A). All four carboxylate ligands are retained, and there are four solvent ligands, two more than for Mn[II] and Cd[II], which is consistent for the coordination geometry of Sm[III]. The longer average metal−ligand distance in this structure compared to those in MnP−Mn[II] and MnP−Cd[II] also supports the presence of Sm[III] with an ionic radius of 1.08 Å in the octacoordinate state (*42*). The side chains of Glu39 and Arg42 are in only one conformation with the former in an open conformation and the latter in its compound I conformation. The solvent structure differs near the metal-binding site, and there is no second metal binding near the C-terminus as observed in MnP−Cd[II] structure.

The second data set (MNPSMOX) was collected using the second piece of the MnP−Sm[III] crystal after it had soaked in the mother liquor containing 10 mM sodium oxalate for several hours. The $F_o − F_c$ map of this data set using MnP−Mn[II] coordinates, lacking Mn[II] and its ligands, differs from that described for MNPSM. Most significantly, the density is weak at the metal-binding site (Figure 5B) and the C-terminal region of the polypeptide chain. There are only four interactions possible for this peak (Table 2 and Figure 5B). Two of the four carboxylates, Glu35 and Glu39, are oriented away from the metal-binding site with distances of 3.47 and 3.57 Å, respectively. This is very similar to the situation observed in the structure of the D179N mutant, which lacks a metal ion (*23*). Soaking the crystal in a sodium oxalate solution resulted in the removal of bound Sm[III]; the site is then occupied by either a water molecule or a sodium ion. No ternary complex containing oxalate was observed. These observations are consistent with ^{1}H NMR data for MnP−lanthanide complexes incubated with oxalate (*30*).

Our observations suggest that the Sm[III] ion in the oxalate-soaked crystal is removed from the active site by oxalate chelation. To test this possibility, we attempted to resubstitute Sm[III] in the crystal used to collect the MNPSMOX data set. The crystal was retrieved and thawed in the mother liquor (MnP crystals are very stable and can withstand a few cycles of freeze−thaw treatment). Small aliquots of the SmCl$_3$ solution were slowly added until the final concentration reached ∼5 mM. The crystal was soaked for several hours and flash-frozen, and a new 1.7 Å data set (MNPOXSM) was collected. Previous exposure of the crystal to X-rays and the freeze−thaw treatment caused a small deterioration, resulting in a higher mosaic content and lower resolution. Nevertheless, the $F_o − F_c$ omit map of this data set exhibited features similar to those observed in the MNPSM map, indicating the resubstitution of Sm[III] in the metal-binding site with >30σ density at the Mn-binding site (Table 2 and Figure 5C). Thus, removal of Sm[III] from the Mn-binding site was accomplished without the formation of a discernible ternary complex containing oxalate. Replacement of the metal in the site indicated that no permanent alteration in the site was caused by the treatment. These results suggest reversible binding of the free Mn[II] substrate to the enzyme and the role of chelators in the release of the Mn[III] product during MnP turnover confirming earlier work (*14*).

The direct observation of Mn[II], Cd[II], and Sm[III] binding in the crystal structure indicates that the Mn-binding site is able to bind reversibly both divalent and trivalent cations with sufficiently high affinity, in accordance with inhibition and ^{1}H NMR studies (*30*) (H. L. Youngs, data not shown). Mn[II] is not released in the presence of oxalate, as the Mn-binding site is indistinguishable in oxalate-free and oxalate-soaked MnP−Mn[II] structures (data not shown), suggesting that no ternary MnP−Mn[II]−oxalate complex is formed and the unchelated Mn[II] binds to the enzyme. However, the observation that Sm[III] can be removed from MnP by oxalate suggests that Mn[III] can be similarly chelated, consistent with kinetic studies (*14*) and the ^{1}H NMR study of MnP complexes with Gd[III] and Cs[III] (*30*). However, no ternary MnP−Sm[III]−oxalate complex was observed in the crystal structure. While lanthanides may mimic the charge of Mn[III], they are quite different in size (*33*) and, as we present here, coordination preference. Thus, any conclusions regarding Mn chemistry based on metal substitutions are tentative. If such a ternary
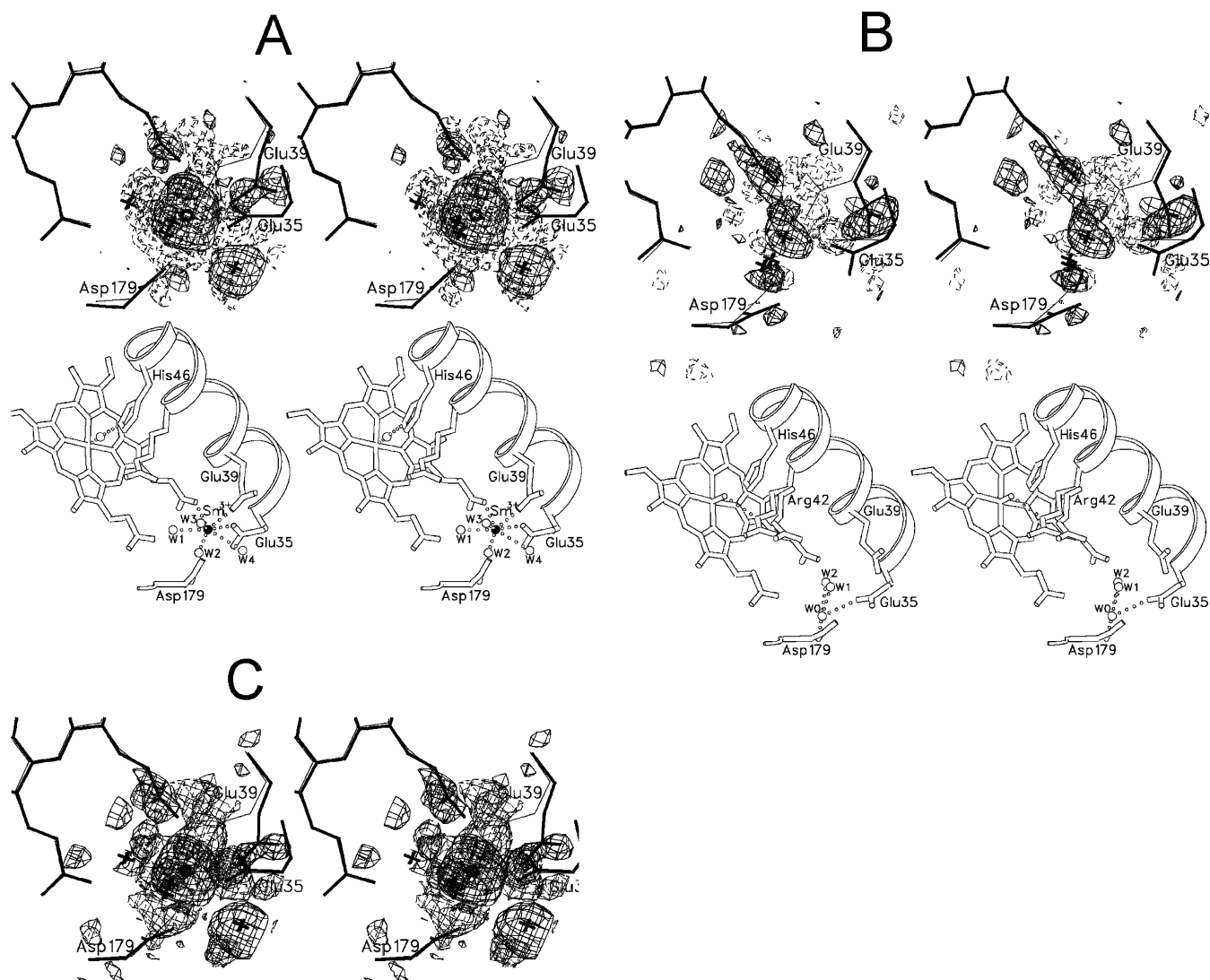
FIGURE 5: (A) Stereoview of the $F_o - F_c$ map at the Mn-binding site (top). The map was calculated using the MNPSM data set and the MnP−Mn^{II} model without Mn^{II}. The models of both MnP−Mn^{II} (thin lines) and refined MnP−Sm^{III} (thick lines) are superimposed. The map is contoured at $\pm 3\sigma$, and the positive peak is stronger than 35σ. Stereoview of the Sm^{III}-bound structure near the Mn-binding site (bottom). The metal is still octacoordinated, with two additional water ligands. There is rearrangement of some protein side chain ligands, but all are in a single conformation. (B) Stereoview of the $F_o - F_c$ map at the Mn-binding site (top). The map was calculated using the MNPSMOX (MnP−Sm^{III} crystal treated with oxalate) data set and the MnP−Mn^{II} model without Mn^{II}. The models of both MnP−Mn^{II} (thin lines) and refined metal-free MnP (thick lines) are superimposed. The map is contoured at $\pm 3\sigma$, and the positive peak at the Mn-binding site is ~6σ, indicating that the site lacks metal. Stereoview of the metal-free structure near the Mn-binding site (bottom). The peak at the Mn-binding site shows only four interactions, two amino acid side chains and two waters. This site is also modeled as water (W0). There is a major rearrangement of protein side chain ligands due to lack of metal, which is reminiscent of the active site mutant structures lacking Mn^{II} (*21, 23*). (C) Stereoview of the $F_o - F_c$ map at the Mn-binding site. The map was calculated using the MNPOXSM data set and the MnP−Mn^{II} model without Mn^{II}. The models of both MnP−Mn^{II} (thin lines) and refined Sm^{III}-resubstituted MnP (the oxalate-treated crystal MnP resoaked in Sm^{III}; thick lines) are superimposed. The map is contoured at $\pm 3\sigma$, and the positive peak is stronger than 30σ, indicating rebinding of Sm^{III}. This is also supported by octacoordination of the site with the same ligation as in the MnP−Sm^{III} structure refined with the MNPSM data set. The X's in the various diagrams represent solvent molecules.

complex forms, it is extremely short-lived and easily disrupted and may be dependent on pH.

REFERENCES

1. Buswell, J. A., and Odier, E. (1987) Lignin Biodegradation, *CRC Crit. Rev. Biotechnol. 6*, 1−60.

2. Kirk, T. K., and Farrell, R. L. (1987) Enzymatic combustion: The microbial degradation of lignin, *Annu. Rev. Microbiol. 41*, 465−505.

3. Gold, M. H., Wariishi, H., and Valli, K. (1989) Extracellular peroxidases involved in lignin degradation by the white rot basidiomycete *Phanerochaete chrysosporium*, *ACS Symp. Ser. 389*, 127−140.

4. Gold, M. H., and Alic, M. (1993) Molecular biology of the lignin-degrading basidiomycete *Phanerochaete chrysosporium*, *Microbiol. Rev. 57*, 605−622.

5. Bumpus, J. A., and Aust, S. D. (1989) Biodegradation of environmental pollutants by the white rot fungus *Phanerochaete chrysosporium*: Involvement of the lignin degrading system, *BioEssays 6*, 166−170.

6. Hammel, K. E. (1989) Organopollutant degradation by ligninolytic fungi, *Enzyme Microb. Technol. 11*, 776−777.

7. Valli, K., Brock, B. J., Joshi, D. K., and Gold, M. H. (1992) Degradation of 2,4-dinitrotoluene by the lignin-degrading fungus *Phanerochaete chrysosporium*, *Appl. Environ. Microbiol. 58*, 221−228.

8. Valli, K., Wariishi, H., and Gold, M. H. (1992) Degradation of 2,7-dichlorodibenzo-p-dioxin by the lignin-degrading basidi-

omycete *Phanerochaete chrysosporium*, *J. Bacteriol. 174*, 2131–2137.

9. Reddy, G. V., and Gold, M. H. (2000) Degradation of pentachlorophenol by *Phanerochaete chrysosporium*: Intermediates and reactions involved, *Microbiology 146* (Part 2), 405–413.

10. Kuwahara, M., Glenn, J. K., Morgan, M. A., and Gold, M. H. (1984) Separation and characterization of two extracellular H_2O_2-dependent oxidases from ligninolytic cultures of *Phanerochaete chrysosporium*, *FEBS Lett. 169*, 247–250.

11. Perie, F. H., Sheng, D., and Gold, M. H. (1996) Purification and characterization of two manganese peroxidase isozymes from the white-rot basidiomycete *Dichomitus squalens*, *Biochim. Biophys. Acta 1297*, 139–148.

12. Glenn, J. K., and Gold, M. H. (1985) Purification and characterization of an extracellular Mn(II)-dependent peroxidase from the lignin-degrading basidiomycete *Phanerochaete chrysosporium*, *Arch. Biochem. Biophys. 242*, 329–341.

13. Glenn, J. K., Akileswaran, L., and Gold, M. H. (1986) Mn(II) oxidation is the principal function of the extracellular Mn-peroxidase from *Phanerochaete chrysosporium*, *Arch. Biochem. Biophys. 251*, 688–696.

14. Wariishi, H., Valli, K., and Gold, M. H. (1992) Manganese(II) oxidation by manganese peroxidase from the basidiomycete *Phanerochaete chrysosporium*. Kinetic mechanism and role of chelators, *J. Biol. Chem. 267*, 23688–23695.

15. Gold, M. H., Youngs, H. L., and Sollewijn Gelpke, M. D. (2000) Manganese peroxidase, in *Manganese and Its Role in Biological Processes* (Sigel, A., and Sigel, H., Eds.) Marcel Dekker, New York.

16. Sundaramoorthy, M., Kishi, K., Gold, M. H., and Poulos, T. L. (1994) The crystal structure of manganese peroxidase from *Phanerochaete chrysosporium* at 2.06-Å resolution, *J. Biol. Chem. 269*, 32759–32767.

17. Kishi, K., Kusters-van Someren, M., Mayfield, M. B., Sun, J., Loehr, T. M., and Gold, M. H. (1996) Characterization of manganese(II) binding site mutants of manganese peroxidase, *Biochemistry 35*, 8986–8994.

18. Kusters-van Someren, M., Kishi, K., Lundell, T., and Gold, M. H. (1995) The manganese binding site of manganese peroxidase: Characterization of an Asp179Asn site-directed mutant protein, *Biochemistry 34*, 10620–10627.

19. Youngs, H. L., Sundaramoorthy, M., and Gold, M. H. (2000) Effects of cadmium on manganese peroxidase competitive inhibition of MnII oxidation and thermal stabilization of the enzyme, *Eur. J. Biochem. 267*, 1761–1769.

20. Sollewijn Gelpke, M. D., Moenne-Loccoz, P., and Gold, M. H. (1999) Arginine 177 is involved in Mn(II) binding by manganese peroxidase, *Biochemistry 38*, 11482–11489.

21. Youngs, H. L., Sollewijn Gelpke, M. D., Li, D., Sundaramoorthy, M., and Gold, M. H. (2001) The role of Glu39 in MnII binding and oxidation by manganese peroxidase from *Phanerochaete chrysosporium*, *Biochemistry 40*, 2243–2250.

22. Whitwam, R. E., Brown, K. R., Musick, M., Natan, M. J., and Tien, M. (1997) Mutagenesis of the Mn^{2+}-binding site of manganese peroxidase affects oxidation of Mn^{2+} by both compound I and compound II, *Biochemistry 36*, 9766–9773.

23. Sundaramoorthy, M., Kishi, K., Gold, M. H., and Poulos, T. L. (1997) Crystal structures of substrate binding site mutants of manganese peroxidase, *J. Biol. Chem. 272*, 17574–17580 [erratum, (1997) *J. Biol. Chem. 272* (41), 26072].

24. Wariishi, H., Valli, K., and Gold, M. H. (1991) *In vitro* depolymerization of lignin by manganese peroxidase of *Phanerochaete chrysosporium*, *Biochem. Biophys. Res. Commun. 176*, 269–275.

25. Popp, J. L., and Kirk, T. K. (1991) Oxidation of methoxybenzenes by manganese peroxidase and by Mn^{3+}, *Arch. Biochem. Biophys. 288*, 145–148.

26. Tuor, U., Wariishi, H., Shoemaker, H. E., and Gold, M. H. (1992) Oxidation of phenolic arylglycerol β-aryl ether lignin model compounds by manganese peroxidase from *Phanerochaete chrysosporium*: Oxidative cleavage of an α-carbonyl model compound, *Biochemistry 31*, 4986–4995.

27. Kishi, K., Wariishi, H., Marquez, L., Dunford, H. B., and Gold, M. H. (1994) Mechanism of manganese peroxidase compound II reduction: Effect of organic acid chelators and pH, *Biochemistry 33*, 8694–8701.

28. Wariishi, H., Akileswaran, L., and Gold, M. H. (1988) Manganese peroxidase from the basidiomycete *Phanerochaete chrysosporium*: Spectral characterization of the oxidized states and the catalytic cycle, *Biochemistry 27*, 5365–5370.

29. Banci, L., Ciofi-Baffoni, S., and Tien, M. (1999) Lignin and Mn peroxidase-catalyzed oxidation of phenolic lignin oligomers, *Biochemistry 38*, 3205–3210.

30. Banci, L., Bertini, I., Dal Pozzo, L., Del Conte, R., and Tien, M. (1998) Monitoring the role of oxalate in manganese peroxidase, *Biochemistry 37*, 9009–9015.

31. Kuan, I. C., and Tien, M. (1993) Stimulation of Mn peroxidase activity: A possible role for oxalate in lignin biodegradation, *Proc. Natl. Acad. Sci. U.S.A. 90*, 1242–1246.

32. Harris, R. Z., Wariishi, H., Gold, M. H., and Ortiz de Montellano, P. R. (1991) The catalytic site of manganese peroxidase. Regiospecific addition of sodium azide and alkylhydrazines to the heme group, *J. Biol. Chem. 266*, 8751–8758.

33. Cotton, F. A., and Wilkinson, G. (1988) *Advanced Inorganic Chemistry*, 5th ed., John Wiley, New York.

34. Sundaramoorthy, M., Kishi, K., Gold, M. H., and Poulos, T. L. (1994) Preliminary crystallographic analysis of manganese peroxidase from *Phanerochaete chrysosporium*, *J. Mol. Biol. 238*, 845–848.

35. Howard, A. J., Gilliland, G. L., Finzel, B. F., Poulos, T. L., Olendorf, D. H., and Salemme, F. R. (1987) The use of an imaging proportional counter in macromolecular crystallography, *J. Appl. Crystallogr. 20*, 383–387.

36. Otwinowski, Z., and Minor, W. (1997) Processing of X-ray diffraction data collected in oscillation method, *Methods Enzymol. 276*, 307–326.

37. Brunger, A. T. (1992) *X-PLOR Manual Version 3.1: A system for X-ray Crystallography and NMR*, Yale University Press, New Haven, CT.

38. Sheldrick, G. M., and Scheider, T. R. (1997) SHELXL: High-resolution refinement, *Methods Enzymol. 277*, 319–343.

39. Jones, T. A. (1978) A graphics model building and refinement system for macromolecules, *J. Appl. Crystallogr. 11*, 268–272.

40. Evans, S. V. (1993) SETOR: Hardware-lighted three-dimensional solid model representation of macromolecules, *J. Mol. Graphics 11*, 134–138.

41. Bonagura, C. A., Bhaskar, B., Shimizu, H., Li, H., Sundaramoorthy, M., McRee, D. E., Goodin, D. B., and Poulos, T. L. (2003) High-resolution crystal structures and spectroscopy of native and compound I cytochrome *c* peroxidase, *Biochemistry 42*, 5600–5608.

42. Shannon, R. D. (1976) Revised effective ionic radii and systematic studies of interatomic distances in halides and chalgogenides, *Acta Crystallogr. A32*, 751–767.

43. Toon, S. P., Ghirardi, M., Mohanty, P., and Seibert, M. (1995) Cadmium inhibition of O_2 evolution and electron transport in isolated photosystem II membranes, *Plant Physiol. 108* (Suppl. 2), 89.

44. Oxenrider, K. A., and Kennelly, P. J. (1993) A protein-serine phosphatase from the halophilic archaeon *Haloferax volcanii*, *Biochem. Biophys. Res. Commun. 194*, 1330–1335.

45. Perry, R. D., and Silver, S. (1992) Cadmium and manganese transport in *Staphylococcus aureus* membrane vesicles, *J. Bacteriol. 150*, 973–976.

46. Laddaga, R. A., Bessen, R., and Silver, S. (1985) Cadmium-resistant mutant of *Bacillus subtilis* 168 with reduced cadmium transport, *J. Bacteriol. 162*, 1106–1110.

47. Trevors, J. T., Stratton, G., and Gadd, G. (1986) Cadmium transport resistance and toxicity in bacteria, algae, and fungi, *Can. J. Microbiol. 32*, 447–464.

48. Mauk, M. R., Kishi, K., Gold, M. H., and Mauk, A. G. (1998) pH-linked binding of Mn(II) to manganese peroxidase, *Biochemistry 37*, 6767–6771.